

Wasserstein Distances Made Explainable: Insights into Dataset Shifts and Transport Phenomena

Philip Naumann, Jacob Kauffmann, Grégoire Montavon

Abstract—Wasserstein distances provide a powerful framework for comparing data distributions. They can be used to analyze processes over time or to detect inhomogeneities within data. However, simply calculating the Wasserstein distance or analyzing the corresponding transport map (or coupling) may not be sufficient for understanding what factors contribute to a high or low Wasserstein distance. In this work, we propose a novel solution based on Explainable AI that allows us to efficiently and accurately attribute Wasserstein distances to various data components, including data subgroups, input features, or interpretable subspaces. Our method achieves high accuracy across diverse datasets and Wasserstein distance specifications, and its practical utility is demonstrated in two use cases.

Index Terms—Explainable AI, Wasserstein Distances, Transport Phenomena, Dataset Shifts, Attribution

I. INTRODUCTION

IN many fields of research, it is necessary to analyze data at the population level. For example, when analyzing chemical reactions or transport phenomena, one typically cannot track every single atom of the physical system of interest and must rely on densities instead. Similarly, when trying to characterize a medical disease, one may not have access to each patient in multiple health states, but only to non-overlapping cohorts of healthy and unhealthy patients. As another example, complex processes that unfold over time (e.g. the spread of an epidemic or the development of biological cells [1]) may only be analyzable at discrete points in time without the ability to trace their detailed temporal evolution.

The Wasserstein distance is a popular and theoretically sound tool for making comparisons at the distribution level. It has its roots in Optimal Transport (OT) [2]–[4], a field concerned with finding cost-minimizing couplings between source and target distributions. The Wasserstein distance can be defined as the result of the optimization problem:

$$\mathcal{W}_p(\mu, \nu) = \inf_{\gamma \in \Gamma(\mu, \nu)} (\mathbb{E}_{(x,y) \sim \gamma} \|x - y\|_q^p)^{1/p} \quad (1)$$

where μ and ν are the two data distributions, $\Gamma(\mu, \nu)$ is the set of all possible couplings γ between them, and $p \geq 1$ is a

hyperparameter that emphasizes penalizing large distances. The minimization objective in Eq. (1) can be interpreted as applying a least-action principle in determining how to match points from the two distributions. Moreover, regularized formulations such as Sinkhorn [5] are also common in practice.

When interested specifically in understanding the nature of the distribution shift, looking at the Wasserstein distance itself provides only limited insight. It only measures the extent to which the distributions μ and ν differ without highlighting the relevant input features or data points. The coupling (or transport map) γ^* obtained as a byproduct of calculating the Wasserstein distance using Eq. (1) can provide further insight into the dataset shift (e.g. [6]). Yet, it still does not specifically pinpoint which part of the data or which input features are genuinely responsible for the low or high Wasserstein distance (cf. Supplementary Note A).

In this work, we propose to address the question of what in the data contributes to the Wasserstein distance between distributions using the tools of Explainable AI (XAI). Explainable AI [7]–[10] is a growing subfield of Machine Learning (ML) that aims to reveal the complex inner-workings of black-box ML models, whether it is to detect flaws in their decision strategy [11]–[13], or provide novel insights [14]–[17]. Methods such as Shapley values [18], [19] or Layer-wise Relevance Propagation (LRP) [20], [21], have been successful in attributing the predictions of a wide variety of popular ML models in terms of input features. To the best of our knowledge, there have been no systematic studies on how to explain the distance between data, especially if distances are not considered at the single-instance level, but at the level of a whole distribution (e.g. the Wasserstein distance).

We propose a new set of Explainable AI techniques referred to together as “WaX” (or ‘Wasserstein distances made explainable’) focused on attributing the Wasserstein distance in terms of various aspects of the data, such as individual data points or input features (see Figs. 1 and 2 and Section III). Our proposed method is grounded in the framework of LRP, expressing the Wasserstein distance as a neural network and explaining it by reverse propagating in that graph. The proposed approach satisfies standard axiomatic properties of explanations, such as conservation, and demonstrates broad applicability by supporting both classical Wasserstein distances and their Sinkhorn-regularized variants [5]. Additionally, it accommodates instance-wise comparisons using the general class of Minkowski distances, which includes the Euclidean distance as a special case. Our method also integrates with subspace analysis methods (see Section V), thereby instantiating

P. Naumann is with BIFOLD – Berlin Institute for the Foundations of Learning and Data, 10587 Berlin, Germany, and the Department of Electrical Engineering and Computer Science, Technische Universität Berlin, 10587 Berlin, Germany

J. Kauffmann is with BIFOLD – Berlin Institute for the Foundations of Learning and Data, 10587 Berlin, Germany, and the Department of Electrical Engineering and Computer Science, Technische Universität Berlin, 10587 Berlin, Germany

G. Montavon is with BIFOLD – Berlin Institute for the Foundations of Learning and Data, 10587 Berlin, Germany, and the Charité – Universitätsmedizin Berlin, 10117 Berlin, Germany. E-mail: gregoire.montavon@charite.de.

(Corresponding Author: Grégoire Montavon)

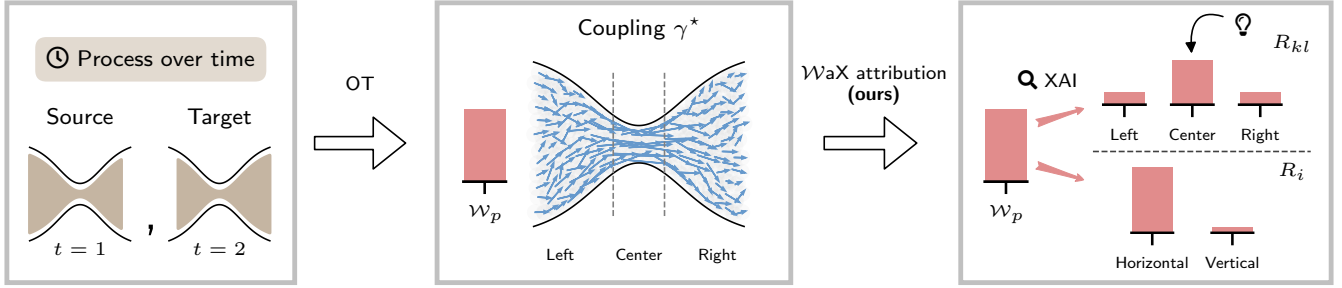


Fig. 1. High-level illustration of WaX, which goes beyond a classical inspection of the Wasserstein-derived transport map γ^* , by attributing the Wasserstein distance on data points and input features. In this example, a fluid moves rightward and is observed at times $t = 1$ and $t = 2$. This phenomenon is represented by a Wasserstein model ($p = 3, q = 2$). WaX identifies the bottleneck at the center as the primary contributor to the high Wasserstein distance—something that is not easily detectable and quantifiable from analyzing the transport map alone. In Supplementary Note A, we provide further examples highlighting how using WaX and simply analyzing the transport map strongly differ in their sensitivity to different Wasserstein model specifications.

“Concept-based XAI” [22]–[24] to the problem of explaining Wasserstein distances.

Through quantitative evaluations on several datasets and Wasserstein distance specifications, we show that our method consistently outperforms a representative set of baseline methods (see Section IV). Furthermore, the practical utility of our method is demonstrated in two use cases (see Sections VI and VII), where it provides insight into complex, nonlinear transport phenomena and helps to navigate differences between large multimodal image datasets. Overall, our method offers capabilities that go well beyond classical statistical analysis or manual inspection of the data.

II. RELATED WORK

Causal Models of Distribution Shifts: Dealing with distribution shifts is a well-known problem in machine learning [25], [26]. Substantial research has focused on better handling (e.g. [27]) and understanding these shifts. One approach involves characterizing distribution shifts through the lens of causal relationships specified via conditional distributions [28]. Within this framework, the Kullback-Leibler Divergence (KLD) can be used to quantify the magnitude of the shift, and Shapley values help to attribute this divergence back to input variables. In contrast, our work uses the Wasserstein distance as a more *direct* distribution shift model from which those can be more directly characterized, as demonstrated in Section IV-B.

Interpreting OT Maps: Another related line of work uses the OT map to retrieve information about the modeled shift. Kulinski *et al.* [6] propose two methods for this purpose: k -sparse and k -cluster maps. The former expresses the k most relevant shift features as a new transport map, which they find by looking at the mean shift strengths between the distributions and sorting them according to their strength. The k -cluster maps model heterogeneous shifts using k -means clustering on the column-wise concatenated source and transport vectors. They aim to detect sub-shifts, which are then expressed through individual transport maps. Another related work [29] also uses the OT map to interpret distribution shifts in classification datasets by comparing distances of farthest and closest examples. Unlike the above works, our approach

does not explain distribution shifts based on the Wasserstein-derived transport map, but directly based on the Wasserstein *distance* (cf. Fig. 1). This enables us to frame the explanation task as an attribution problem (cf. [18], [20], [30]), and derive relevance scores that directly capture the effect of adding or removing input features on the distance between distributions (see Section IV-A).

Intrinsically Interpretable OT Models: Some works have focused on making OT itself more interpretable through specific reformulations of the OT problem that include anchors or feature sparsity [31], [32]. In contrast to these works, we propose a post-hoc explanation method that can readily apply to popular Wasserstein distance formulations. In particular, our method can explain transport phenomena without introducing specific modeling constraints.

Explaining Robustness under Distribution Shift: Recent advances focus on explaining the behavior of (classification) ML models under distribution shifts by incorporating data relationships. Zhang *et al.* [33] extend the work of [28] by focusing on explaining the performance drop of an ML model due to an underlying distribution shift. Using a causal graph and Shapley values, they trace the identified causes back to the data distributions. Recent work used the OT coupling to find features likely to affect a classifier’s performance [34]. They also use Shapley values to assess the contribution of each feature to the shift-induced performance loss. Unlike these works, our approach does not explain the behavior of an ML model under distribution shifts, but focuses on characterizing the shift itself. In the context of tabular data, Liu *et al.* [35] argue that not all distribution shifts are equal. Different variants, stemming from various causes, each require special attention. For this reason, they propose a benchmark that focuses on “(Y|X)-shifts”, which they consider the most critical in affecting ML performance. Complementary to [35], another benchmark has been proposed by Gardner *et al.* [36]. Our work differs in its goals by attempting to characterize all types of shifts, and methodologically by identifying each feature’s contribution.

Explaining Distance-Based Models: Several papers have addressed the technical question of explaining distances in ML models. Specific instantiations have been proposed in the context of anomaly [37] and clustering models [38], both of

which study the particular geometry of the distance function and the composition of these in the prediction model. Our work differs in that we consider distances not only at the instance level, but also at the level of the entire data distribution.

OT as a Tool for Explainability: The intersection of Explainable AI and optimal transport has been explored for broader goals. These include generating counterfactual explanations at the distribution level [39], making ML models more interpretable [40], and evaluating XAI methods themselves [41]. In all cases, the goals of these works diverge significantly from our main goal, which is to characterize distribution shifts and transport phenomena.

III. WASSERSTEIN DISTANCES MADE EXPLAINABLE

We now introduce our proposed method, called ‘‘WaX’’, for explaining Wasserstein distances in terms of data points and input features. WaX applies to a fairly general class of Wasserstein distances (\mathcal{W}_p with arbitrary exponent p and the class of Minkowski distances between pairs of points). It also allows the user to flexibly choose the basis for interpretability, as it can produce an attribution in terms of individual instances, input features, latent subspaces (cf. Section V), or combinations of these. Technically, WaX follows a *neuralization-propagation* approach (cf. [38]), where the quantity to be explained, here the Wasserstein distance, is first rewritten as a functionally equivalent neural network, which then guides the explanation process through a purposefully designed backward pass¹. The WaX procedure is illustrated in Fig. 2 and described in detail below. In the following, we assume that the distributions μ and ν are empirical, i.e. formally defined as $\mu(\xi) = \frac{1}{N} \sum_{k=1}^N \delta(\xi - x_k)$, $\nu(y) = \frac{1}{M} \sum_{l=1}^M \delta(y - y_l)$, where δ is the Dirac delta function, and $x_k \in \mathbb{R}^d$ and $y_l \in \mathbb{R}^d$ are data points. The coupling distribution γ can then be represented as a matrix of size $N \times M$.

Neuralization: We first identify a neural network structure that reproduces the Wasserstein distance \mathcal{W}_p from the two distributions μ and ν . Specifically, we propose to decompose the Wasserstein distance in Eq. (1) into two layers of computations:

$$z_{kl} = \|x_k - y_l\|_q \quad (2a)$$

$$\mathcal{W}_p = \left(\sum_{kl} \gamma_{kl}^* \cdot z_{kl}^p \right)^{1/p} \quad (2b)$$

The first layer computes the differences between pairs of instances from the two distributions. The second layer applies a norm (weighted by the optimal coupling γ^*) over the pairwise distances computed in the previous layer. The difference vectors $(x_k - y_l)$ provide the directionality in input space necessary to identify the relevant input features. Similarly, the norm over pairwise distances weighted by the coupling probabilities γ_{kl}^* helps to identify relevant instances. We note that the *primal* formulation of optimal transport that our neural network replicates is crucial for explanation purposes: distances between

instance pairs appear explicitly in the primal, and the latter is supported by a coupling matrix γ^* that is instrumental in separating the few relevant instance pairs from the many irrelevant ones.²

Propagation: Leveraging the neural network structure defined above, our method proceeds by reverse-propagating the output \mathcal{W}_p through the layers to identify the relevant instances and input features. The first propagation step decomposes \mathcal{W}_p into contributions of instance pairs (denoted by R_{kl}). The second step further propagates these contributions to identify the feature contributions R_i . Specifically, our WaX method defines the following propagation equations:

$$R_{kl} = \frac{\gamma_{kl}^* \cdot z_{kl}^\alpha}{\sum_{kl} \gamma_{kl}^* \cdot z_{kl}^\alpha} \mathcal{W}_p \quad (3a)$$

$$R_i = \sum_{kl} \frac{|x_{ki} - y_{li}|^\beta}{\sum_i |x_{ki} - y_{li}|^\beta} R_{kl} \quad (3b)$$

where α and β are two hyperparameters to be set. It is easy to see from the above equations that the LRP rules satisfy the conservation property $\sum_i R_i = \sum_{kl} R_{kl} = \mathcal{W}_p$. Our reverse propagation approach can be seen as an instantiation of LRP to the specific neural network identified in the neuralization step. Unlike other attribution techniques, e.g. based on feature removal [18], the LRP approach requires only a single evaluation of the prediction function and also avoids the need to address the question of how to remove input features.

We now ask what good hyperparameters α and β are for these rules. To this end, we first establish a connection with gradient-based attribution (cf. [43]):

Proposition 1. *When choosing $\alpha = p$, the relevance scores R_{kl} of pairs of points can be expressed as the gradient computation $R_{kl} = (\partial \mathcal{W}_p / \partial z_{kl}) \cdot z_{kl}$, where we treat γ^* as a constant.*

Proposition 2. *When choosing $\alpha = p$ and $\beta = q$, the relevance scores R_i of the input features can be expressed as the gradient computation $R_i = (\partial \mathcal{W}_p / \partial x_{:,i})^\top x_{:,i} + (\partial \mathcal{W}_p / \partial y_{:,i})^\top y_{:,i}$, where γ^* is again treated as constant.*

Proofs are given in Supplementary Note B. In other words, if we set $\alpha = p$ and $\beta = q$, the LRP rules have a gradient interpretation, i.e. Gradient \times Input (GI). For large values of p and q (e.g. the extreme cases $p, q = \infty$), the gradient becomes discontinuous and gives an implausible explanation. We settle on the heuristic $\alpha = p$ and $\beta = \min(p + 2, q)$, assuming $p \ll \infty$, and use it in all our evaluations. A systematic analysis of different α, β combinations for the ‘Mice’ dataset is given in Supplementary Note C and supports this heuristic.

Finally, we briefly discuss the computational requirements of our method. A naive implementation would require maintaining a tensor of size $N \times M \times d$ storing the relevance scores for

¹Explainable AI methods such as LRP [20], guided GradCAM [42], or DeepSHAP [19] all require the ML model to be a neural network, and they explain by performing a backward pass in the neural network.

²In comparison to the primal, the input directionality of the Wasserstein *dual*’s Kantorovich potentials is more difficult to capture. The joint distribution $\mu \times \nu$ over which these potentials are integrated does not easily allow for separating relevant from irrelevant instance pairs.

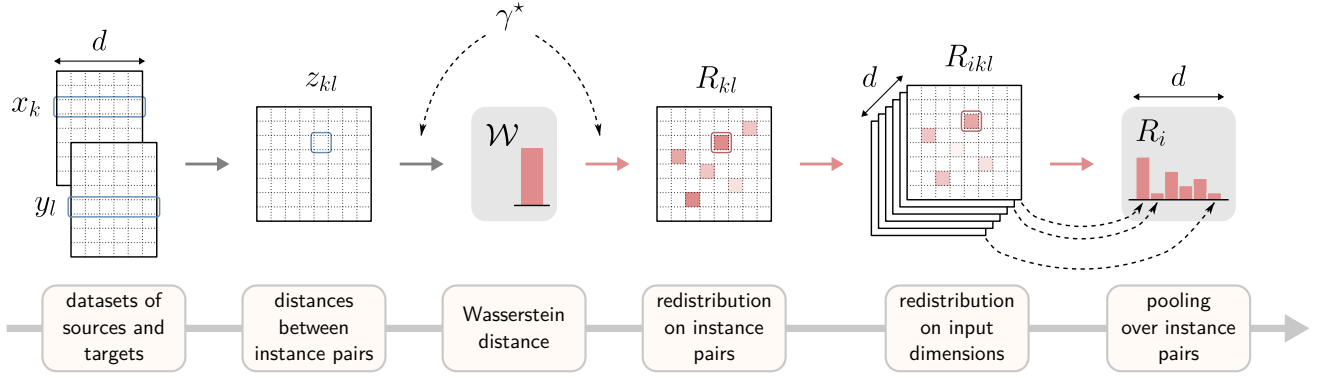


Fig. 2. Diagram of WaX’s computational workflow. The Wasserstein distance is viewed as a two-layer network with the coupling fixed to its optimum γ^* . Explanation proceeds through a backward pass, leading first to an attribution on instance pairs, and then on input features.

each explanation (as shown in Fig. 2). This can be bypassed for the case $\alpha = p$ and $\beta = q$ by using the gradient formulations of Propositions 1 and 2. For the more general case where $\alpha \neq p$ or $\beta \neq q$, we can use a “detach trick” [9], [44] where some terms of the forward computation are set to constants. Specifically, we replace Eq. (2a) by:

$$z_{kl} = \|x_k - y_l\|_\beta \cdot \left[\frac{\|x_k - y_l\|_q}{\|x_k - y_l\|_\beta} \right]_{\text{detach}()} \quad (4)$$

and likewise for Eq. (2b). This has the effect of leaving the output of the forward computation unchanged, but making the gradient computations shown in Propositions 1 and 2 coincide with those of LRP shown in Eqs. (3a) and (3b). Furthermore, for the case where the transport is sparse (e.g. classical unregularized transport between distributions with the same number of source and target instances), the structures storing the activations z_{kl} and R_{kl} can be reduced to one-dimensional arrays, further speeding up the computations by a factor N . Overall, our explanation method is fast and can be applied to large transport models involving many data points and input features without incurring any significant computational overhead.

IV. EMPIRICAL EVALUATION

Our evaluation procedure consists of two parts. In the first part, Section IV-A, we focus on testing the ability of our WaX method to faithfully explain any Wasserstein model, whether it is to gain insight into its predictions or reveal its flaws. In Section IV-B, we proceed with a more holistic evaluation, testing the ability of WaX—combined with a suitable Wasserstein model—to identify underlying transport phenomena.

A. Evaluating Explanation Faithfulness

To test the ability of WaX to explain Wasserstein distance models faithfully, we use the Symmetric Relevance Gain (SRG) metric [45]³. We denote by (x_π^+, y_π^+) the dataset of source and

target samples obtained by *retaining* only the π most relevant features according to the explanation. Likewise, we denote by $(x_\pi^\times, y_\pi^\times)$ the dataset formed by *excluding* the π most relevant features according to the explanation. The SRG can then be written as:

$$\text{SRG} = \frac{1}{d+1} \sum_{\pi=0}^d [\mathcal{W}_p(x_\pi^+, y_\pi^+) - \mathcal{W}_p(x_\pi^\times, y_\pi^\times)] \quad (5)$$

where datasets rather than distributions are plugged into \mathcal{W}_p for notational convenience. The SRG intuitively measures the true effect on the Wasserstein distance of adding a feature identified as relevant by the explanation rather than one identified as irrelevant. The higher the SRG, the better the explanation.

We evaluate our method on various specifications of the Wasserstein distance and its underlying Minkowski metric, including popular settings such as $\mathcal{W}_1, \mathcal{W}_2$, and the Euclidean distance between points. Corresponding Wasserstein models were built on various datasets of different sizes and dimensionality. Further details on the datasets and their preprocessing are given in Supplementary Note D.

Baselines: We contribute a simple set of baselines for benchmarking purposes. The first baseline, *MeanShift*, estimates and compares the mean feature values of the distributions, i.e. $R_i = (\mathbb{E}[x] - \mathbb{E}[y])_i^2$. This baseline does not consider the model and only looks at the means of the datasets. The second baseline, *Occlusion*, attributes according to the effect of removing one dimension on the original Wasserstein distance, i.e. $R_i = \mathcal{W}_p(x, y) - \mathcal{W}_p(x_{:, -i}, y_{:, -i})$, where $x_{:, -i}$ denotes the samples after removing the i th dimension (and likewise for y). This baseline is highly localized and cannot comprehend the more global effect of removing multiple input features. Moreover, this baseline requires solving the optimal transport function d times (once for every feature removal), which is computationally expensive for large problems. Our last baseline, *Coupling*, looks at the coupling distribution γ^* obtained as a byproduct of calculating the Wasserstein distance. It attributes the distances (assumed to be Euclidean) between the coupled instances to the input features and averages the results over the data. Up to a global scaling factor on the explanation, this baseline is an ablation of WaX with its hyperparameters fixed to $\alpha = 1$ and $\beta = 2$.

³The SRG is based on the “pixel-flipping” evaluation metric [20], [46] but adapted to produce more robust explanation evaluations.

TABLE I

SRG SCORES OBTAINED BY EACH EXPLANATION METHOD ON VARIOUS WASSERSTEIN DISTANCE MODELS (DIFFERENT VALUES OF p AND q) AND DATASETS. FOR EACH DATASET, WE ALSO SHOW THE NUMBER OF SOURCE AND TARGET DATA POINTS N AND M , AND THE NUMBER OF INPUT FEATURES d . \boxtimes SLOW RUNTIME. \oplus EQUIVALENT UP TO A SCALING FACTOR TO AN ABLATION OF $\mathcal{W}aX$ WITH $\alpha = 1, \beta = 2$. BEST RESULTS ARE SHOWN IN **BOLD**.

\mathcal{W}_p	$\ x - y\ _q$	Dataset	($N / M / d$)	MeanShift	Occlusion \boxtimes	Coupling \oplus	$\mathcal{W}aX$ (ours)
$p = 1$	$q = 2$	Crime	(437 / 1081 / 28)	0.84	0.86	0.91	0.91
		Mice	(628 / 203 / 70)	0.87	1.47	1.47	1.47
		Musks1	(133 / 167 / 166)	0.81	1.99	1.99	1.99
		Robot	(118 / 65 / 90)	-0.21	1.06	1.05	1.05
		Wine	(3781 / 1086 / 12)	1.09	1.08	1.08	1.08
		Wisconsin	(332 / 163 / 30)	1.86	1.86	1.86	1.86
:	$q = 1$	Crime		2.65	2.60	2.55	2.74
		Mice		3.92	6.24	6.20	6.27
		Musks1		5.65	11.67	9.44	11.67
		Robot		3.22	6.89	-0.42	6.89
		Wine		2.61	2.57	2.59	2.61
		Wisconsin		7.29	7.30	7.29	7.30
$p = 2$	$q = 2$	Crime		0.85	0.93	0.91	0.99
		Mice		0.92	1.51	1.51	1.52
		Musks1		0.95	1.88	1.87	1.89
		Robot		0.44	0.67	0.19	0.68
		Wine		1.01	1.04	1.04	1.04
		Wisconsin		1.89	1.90	1.90	1.91
:	$q = \infty$	Crime		0.35	0.58	0.25	0.62
		Mice		0.36	0.56	0.56	0.60
		Musks1		0.26	0.86	0.35	0.93
		Robot		0.17	0.53	0.54	0.86
		Wine		0.46	0.48	0.44	0.50
		Wisconsin		0.53	0.25	0.53	0.57
$p = 10$	$q = 2$	Crime		1.77	3.83	1.32	3.83
		Mice		0.93	1.60	1.55	1.63
		Musks1		0.65	2.18	1.67	2.15
		Robot		5.91	8.18	-4.39	8.16
		Wine		0.89	0.97	0.96	1.00
		Wisconsin		2.08	2.37	2.16	2.38

Results: The results of our evaluation are shown in Table I. We observe that our $\mathcal{W}aX$ method consistently produces the highest SRG scores across Wasserstein models and datasets. This confirms the technical strength of our method, namely its sensitivity to the actual Wasserstein distance model and its ability to attribute the Wasserstein distance comprehensively through its fulfillment of the conservation property (cf. Table II for a technical comparison between methods).

Our method outperforms the *MeanShift* and *Coupling* baselines. *MeanShift* suffers from only looking at the data distributions and being insensitive to the actual Wasserstein distance. Likewise, the coupling distribution γ^* used in the *Coupling* baseline inherits the insensitivity of the transport map to the Wasserstein distance and its parameters (cf. Supplementary Note A). The two baselines perform especially

weakly compared to $\mathcal{W}aX$ when explaining Wasserstein models with high p and q values, as they fail to account for the high sensitivity of these Wasserstein models to specific outlier instances or features. In contrast, $\mathcal{W}aX$ can finely adapt the exposure of the explanation to outliers through a judicious choice of parameters α and β .

$\mathcal{W}aX$ also outperforms the *Occlusion* baseline, despite the latter being much more computationally expensive. By only simulating one feature removal step, *Occlusion* cannot account for the effect on the Wasserstein distance of removing multiple features. The locality of the *Occlusion* is particularly problematic for models with sharp non-linearities near joint feature activations (such as those with large q), whereas $\mathcal{W}aX$ is better equipped to handle these highly nonlinear cases through the capping heuristic for the parameter β and the smoothing it induces on the explanations.

Overall, the results correlate with the fulfillment of the technical desiderata studied in Table II and the empirical performance reported in Table I. Our method, which fulfills all the considered desiderata, also performs the best empirically.

TABLE II

TECHNICAL COMPARISON OF OUR PROPOSED $\mathcal{W}aX$ EXPLANATION METHOD AGAINST A SET OF CONTRIBUTED BASELINES.

Method	Conserving	Model-aware	Efficient
MeanShift	-	-	✓
Occlusion	-	✓	-
Coupling	-	(✓)	✓
$\mathcal{W}aX$ (ours)	✓	✓	✓

B. Characterization of Transport Phenomena

We now examine the ability of $\mathcal{W}aX$, when paired with a suitable Wasserstein distance model, to accurately characterize transport phenomena, specifically the dimensions along

which transport occurs. We first artificially generate transport phenomena with ground-truth from three multivariate time series datasets, ‘Air Quality’, ‘Electricity’, and ‘Appliances’, as described in Supplementary Note D. Denoting the multivariate time series x_1, x_2, \dots with periodicity T , we generate the source and target distributions

$$\begin{aligned} \mathcal{D}_S &= \{(x_{t+kT})\}_{k \in \mathbb{Z}} \\ \mathcal{D}_T &= \{(x_{t+\Delta t+kT})\}_{k \in \mathbb{Z}} \end{aligned}$$

where t is the source time (e.g. 7 am in the morning), $t + \Delta t$ is the target time (e.g. 9 am in the morning, i.e. two hours later), and T is the periodicity of the time series (24 hours in our experiments). We only retain coupled points from the same day, i.e. $0 \leq t < t + \Delta t \leq 23$. A ground-truth estimate of the transport along a specific dimension i can then be obtained by computing:

$$R_i^{(\text{true})} = \mathbb{E}_k[(x_{t+\Delta t+kT,i} - x_{t+kT,i})^2] \quad (6)$$

We set as an objective for $\mathcal{W}aX$ to reconstruct these ground-truth relevance scores, specifically, producing a vector of relevance scores with maximum cosine similarity to the ground-truth, while having only access to samples from the sets $\tilde{\mathcal{D}}_S = \{(x_{t+kT})\}_{k \in \mathcal{K}_1}$ and $\tilde{\mathcal{D}}_T = \{(x_{t+\Delta t+kT})\}_{k \in \mathcal{K}_2}$. Details of the experiment and processing of these datasets are given in Supplementary Notes D and E.

Apart from the time series data, we also use the PLISM [47] histopathology dataset. It consists of a fixed set of patches from various tissue types, each recorded multiple times with different stainings and scanners. We use this natural coupling and evaluate two different staining variations of the same patches and embed these into the latent spaces of the histopathology

foundation models CigaResNet [48], Phikon [49], and UNI [50]. These models differ in recency, size, and performance. The resulting embeddings are each normalized to unit norm.

We consider two variants of $\mathcal{W}aX$: one where the coupling γ^* is the exact solution of Eq. (1), and one where the coupling is set uniform, i.e. fixed to $\gamma_{\text{reg}}^* = \mathbf{1}_{N \times N} / N^2$. This variant can be seen as a limit case of the Sinkhorn [5] distance (a regularized Wasserstein distance) with maximum entropic smoothing.

Baselines: We consider three baselines. The simplest is *Uniform*, which assigns relevance uniformly and constantly as $R_i = 1$. This baseline, therefore, represents an equal impact of all features. We also include *MeanShift*, as already defined in Section IV-A, and a *Logistic* baseline, which derives explanations from a linear classifier $f(x) = w^\top x + b$, trained using logistic regression. Attributions are computed via sensitivity and GI: $R_i^{\nabla^2} = (\partial f / \partial x_i)^2 = w_i^2$ and $R_i^{\text{GI}} = w_i(\mathbb{E}[x] - \mathbb{E}[y])_i$ (cf. Supplementary Note F). The source and target domains are used as a binary classification problem in this case. A particularly interesting aspect about the *MeanShift* and *Logistic* baselines is that they can be seen as specific cases of a recent proposal based on attributing the symmetrized Kullback-Leibler divergence (also known as ‘Jeffrey’s divergence’) $D_{\text{KL}}(\mu, \nu) = D_{\text{KL}}(\mu \parallel \nu) + D_{\text{KL}}(\nu \parallel \mu)$ between the two distributions (cf. Supplementary Note F). A related KLD-based analysis can be found in [28] in the context of causal graphs.

Results: In Table III, we see that $\mathcal{W}aX$ systematically ranks first in characterizing the ground-truth transport phenomena. In particular, our method outperforms *MeanShift*, which represents translations in input space, but no increases/decreases in variance or more complex distortions. These more complex forms of distributional change appear to dominate across

TABLE III

MEAN COSINE SIMILARITIES BETWEEN THE GROUND-TRUTH RELEVANCE SCORES FROM EQ. (6), AND RELEVANCE SCORES COMPUTED BY EACH METHOD. FOR EACH DATASET, WE ALSO SHOW THE MEDIAN NUMBER OF SOURCE AND TARGET DATA POINTS \tilde{N} IN EACH SUBSET $\mathcal{D}_S, \mathcal{D}_T$, AND THE NUMBER OF INPUT FEATURES d . BEST RESULTS ARE SHOWN IN **BOLD**.

Dataset	(\tilde{N} / d)	Uniform	MeanShift	Logistic [∇^2]	Logistic [GI]	$\mathcal{W}aX$ (ours)	
						γ^*	γ_{reg}^*
Air Quality (every 1h)	(363 / 9)	0.83	0.82	0.65	0.47	0.85	0.80
Air Quality (every 2h)	(354 / 9)	0.84	0.87	0.68	0.40	0.91	0.83
Air Quality (every 3h)	(353 / 9)	0.85	0.88	0.69	0.40	0.93	0.87
Air Quality (every 4h)	(349 / 9)	0.86	0.87	0.67	0.40	0.94	0.89
Air Quality (every 5h)	(351 / 9)	0.87	0.92	0.67	0.43	0.95	0.90
Air Quality (every 6h)	(352 / 9)	0.88	0.91	0.67	0.42	0.95	0.91
Electricity (every 1h)	(1213 / 7)	0.84	0.61	0.47	0.43	0.83	0.88
Electricity (every 2h)	(1201 / 7)	0.90	0.68	0.54	0.42	0.86	0.94
Electricity (every 3h)	(1192 / 7)	0.93	0.71	0.55	0.35	0.86	0.96
Electricity (every 4h)	(1191 / 7)	0.94	0.74	0.60	0.42	0.87	0.97
Electricity (every 5h)	(1221 / 7)	0.94	0.75	0.60	0.37	0.88	0.98
Electricity (every 6h)	(1234 / 7)	0.94	0.77	0.61	0.37	0.88	0.98
Appliances (every 1h)	(124 / 25)	0.38	0.28	0.06	0.10	0.51	0.41
Appliances (every 2h)	(121 / 25)	0.47	0.35	0.10	0.14	0.62	0.50
Appliances (every 3h)	(120 / 25)	0.53	0.40	0.15	0.19	0.69	0.56
Appliances (every 4h)	(119 / 25)	0.58	0.43	0.20	0.25	0.74	0.62
Appliances (every 5h)	(119 / 25)	0.62	0.48	0.23	0.29	0.78	0.66
Appliances (every 6h)	(119 / 25)	0.65	0.54	0.26	0.34	0.81	0.69
PLISM (CigaResNet)	(5000 / 512)	0.70	0.90	0.59	0.64	1.00	0.92
PLISM (Phikon)	(5000 / 768)	0.43	0.96	0.90	0.94	1.00	0.92
PLISM (UNI)	(5000 / 1024)	0.83	0.77	0.73	0.75	0.99	0.93

the transport phenomena, and this effect is consistent across various considered delays Δt . The *Logistic* baseline performs significantly worse on this benchmark, regardless of whether sensitivity analysis (∇^2) or Gradient \times Input (GI) is used for the final explanation step. This can be explained by a mismatch between the directions of actual transport and the directions that discriminate between sources and targets. This mismatch can be shown to occur as soon as the source and target distributions are not isotropic. A related phenomenon is discussed in [51]. More generally, classifier-based approaches struggle when the source and target distributions are highly overlapping, which is not a problem for the Wasserstein distance model.

V. SUBSPACE-BASED EXPLANATIONS

We now introduce “ U - $\mathcal{W}aX$ ”: an extension of $\mathcal{W}aX$ aiming at producing a new form of explanation, namely, an attribution of the Wasserstein distance on subspaces of the input domain. These subspaces will be set to be interpreted as abstract concepts describing sub-shifts. The proposed method restricts itself to the specific choice of parameters $p = 2$ and $q = 2$, corresponding to the common \mathcal{W}_2 distance with underlying Euclidean metric for pairwise comparisons. The starting point of U - $\mathcal{W}aX$ is to define an orthogonal matrix U of size $d \times d$ that we decompose column-wise into blocks:

$$U = (U_1 | \dots | U_C | U_\perp) \quad (7)$$

where the first C blocks define C subspaces of the input domain, each associated with a concept, and the last block U_\perp is the orthogonal complement. Note that concepts can be associated with subspaces of potentially different sizes. Under such a decomposition of the input space, we observe that the Wasserstein distance can be expressed as a three-layer neural network:

$$z_{kl}^c = \|U_c^\top (x_k - y_l)\|_2 \quad (8a)$$

$$S_c = \left(\sum_{kl} \gamma_{kl}^* (z_{kl}^c)^2 \right)^{1/2} \quad (8b)$$

$$\mathcal{W}_2 = \left(\sum_c S_c^2 \right)^{1/2} \quad (8c)$$

where the second layer outputs concept-specific scores, and the last layer performs a pooling operation over these concepts. We stress that the output of Eq. (8c) is equivalent to the output of Eq. (2b) with $p = 2$ and $q = 2$, and therefore, we are still considering the same original Wasserstein distance.

This more sophisticated restructuring of the Wasserstein distance allows it to be attributed to the concepts defined by the newly defined subspaces. In particular, we propose an alternate set of LRP rules, which proceeds first by redistribution onto those concepts, Eq. (9a), then the data points, Eq. (9b), and finally the input dimensions Eq. (9c):

$$R_c = \frac{S_c^2}{\sum_c S_c^2} \mathcal{W}_2 \quad (9a)$$

$$R_{kl}^c = \frac{\gamma_{kl}^* (z_{kl}^c)^2}{\sum_{kl} \gamma_{kl}^* (z_{kl}^c)^2} R_c \quad (9b)$$

$$R_i^c = \sum_{kl} \frac{(x_{ki} - y_{li}) \cdot (\hat{x}_{ki} - \hat{y}_{li})}{\sum_i (x_{ki} - y_{li}) \cdot (\hat{x}_{ki} - \hat{y}_{li})} R_{kl}^c \quad (9c)$$

where $(\hat{x}_k - \hat{y}_l) = U_c U_c^\top (x_k - y_l)$. As with standard $\mathcal{W}aX$, the LRP conservation property still holds.

What we have left unanswered so far is how to generate an orthogonal matrix U whose subspaces carry a specific meaning (e.g. a concept or sub-shift). In the following, we extend the approach of [24], which addresses the question of finding those subspaces in the context of neural networks. Inspired by subspace analysis methods such as Independent Component Analysis (ICA), we proceed by associating to each concept c , a tailedness statistic:

$$Q_c = \left(\sum_{kl} \gamma_{kl}^* (z_{kl}^c)^r \right)^{1/r} \quad (10)$$

where $r \geq 2$ is a hyperparameter. Setting r large corresponds to letting the largest distances between coupled points dominate the statistic. Having set the hyperparameter r , we then proceed by searching for the subspaces that maximize the tailedness statistics of each subspace:

$$\max_U \{Q_1 + \dots + Q_C\} \quad (11)$$

subject to U 's orthogonality. Optimization can be achieved by alternating gradient ascent and orthogonalization steps. Note that for the special case where $r = 2$ and $C = 1$, the solution can be more directly found in the eigenvectors of the matrix $\sum_{kl} \gamma_{kl}^* (x_k - y_l)(x_k - y_l)^\top$ (see Supplementary Note G).

It is important to stress that, unlike classical subspace analyses such as PCA and ICA, our proposed U - $\mathcal{W}aX$ does not simply describe the data. Instead, it focuses on directions that are *relevant* to the transport phenomena. Conversely, directions of large variance are ignored by our method if they are present both in the source and target data. Subspace analyses that focus on the target task are a recent direction in Explainable AI (e.g. [24]), and we hereby provide an instantiation of it to the case of Wasserstein distances.

VI. USE CASE 1: EXPLORING AN AGING PHENOMENON

In the following, we will demonstrate how our $\mathcal{W}aX$ framework, in particular U - $\mathcal{W}aX$, can shed light on a real-world transport phenomenon through only accessing data at the distribution level. Specifically, we study the scenario of a heterogeneous cohort observed twice (once at time t , and once at time $t + \tau$), and want to characterize how it evolves in this time interval. We simulate such a scenario using the abalone [52] dataset. The number of rings on an abalone roughly represents its age in years (age \approx rings + 1.5) [52]. We use this relation to generate two subsets of data spanning the ranges 6 to 14 rings and 7 to 15 rings, and sampled in a way that simulates the same cohort being observed twice at a one-year interval (see Supplementary Note D for preprocessing details). We refer to these sets as source and target.

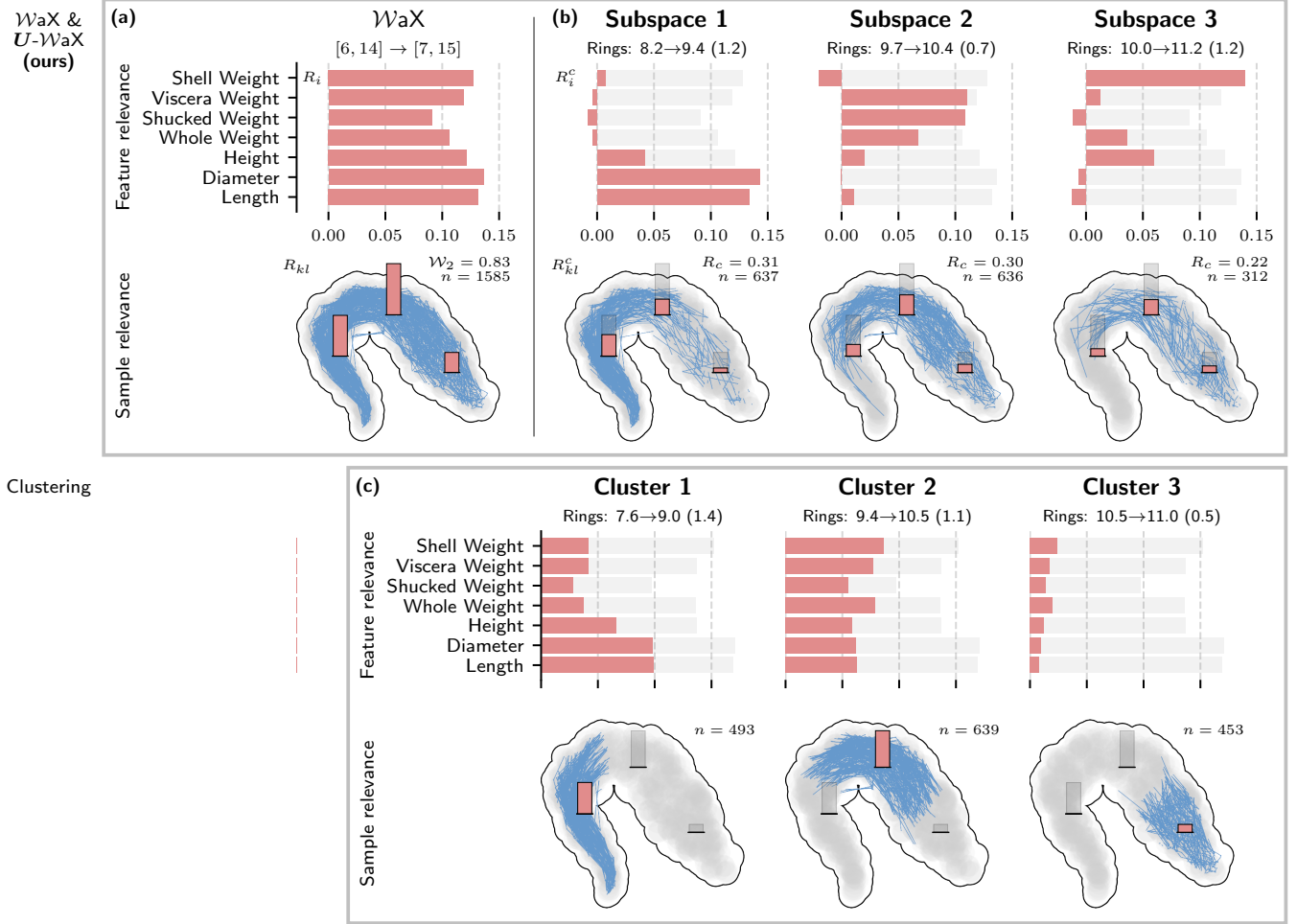


Fig. 3. Insight into an abalone aging process through the WaX and $U-WaX$ methods. The Wasserstein distance models the shift in a simulated abalone cohort measured twice at approximately a one-year interval. (a) Instance-wise (R_{kl}) and feature-wise attributions (R_i) calculated by WaX . (b) Attribution on subspaces (i.e. R_{kl}^c and R_i^c) extracted by $U-WaX$ ($r = 4$). (c) Similar analysis where $U-WaX$ is substituted by a simpler clustering baseline [6] to generate ‘subspaces’. Instance-wise attributions are summarized in three data subgroups based on the cluster assignments of (c) and overlaid on the t-SNE plot of the data. Transport arrows in each t-SNE show the coupled sample pairs that are strongest in the subspace, or assigned to the cluster. The bar sizes indicate the contribution of each data component to the Wasserstein distance.

To comprehend the modeled aging process, we build a Wasserstein distance model between source and target, with $p = 2$ and $q = 2$. The modeled Wasserstein distance subsumes the change in feature space resulting from the cohort aging by one year. We proceed with the application of WaX , which allows us to uncover features that contribute most to the distributional change modeled by the Wasserstein distance. Results are shown in Fig. 3 (a), where vertical and horizontal bars denote instance-wise and feature-wise contributions to the Wasserstein distance, as computed by Eq. (3). The results highlight that all instances and features are relevant to aging.

While the analysis above provides fundamental insight, we note that the simulated abalone cohort is highly heterogeneous, spanning a wide range of ages and containing different abalone subtypes. Aging in this cohort is likely a multifaceted process with distinct subgroups of abalones aging differently. To investigate this hypothesis, we apply our proposed $U-WaX$ analysis and configure it to decompose the Wasserstein distance into three subspaces. The result of this more detailed analysis is

presented in Fig. 3 (b), where vertical and horizontal bars again denote the instance-wise and feature-wise contributions, this time filtered by each subspace, i.e. computed using Eqs. (9b) and (9c), respectively.

Our analysis confirms the multifaceted nature of the modeled aging process, where different subgroups of instances are associated with different features. For example, contrasting subspace S_1 with subspaces S_2 and S_3 reveals that the height, diameter, and length features tend to evolve and contribute distinctly to weight-related features in the overall abalone aging process. This partitioning of features discovered by our analysis coincides with a well-known physical law: weight tends to increase nonlinearly with length or diameter, specifically following some power of these quantities. Concretely, it follows from this law that weight variations associated with a given increase of diameter are significantly bigger in large abalones than in small ones. Lastly, the differences between S_2 and S_3 reveal some heterogeneity in how abalones acquire weight, with weights of different parts of the abalone exhibiting relatively

independent growth. This latter observation could be linked to the manifestation of distinct subtypes among larger abalones, each of which may follow distinct temporal evolutions.

To highlight the unique disentanglement capabilities of U - $\mathcal{W}aX$, we show for comparison a similar analysis where it is substituted by the clustering approach proposed in [6]. Their algorithm first computes the optimal transport map between source and target distributions. It then performs k -means clustering on the column-wise concatenated source x and transported y vectors (x, y) , resulting in a set of prototypes $(m_c^x, m_c^y)_{c=1}^C$, where the differences $\delta_c = m_c^y - m_c^x$ model the mean shift in each cluster. For comparability with U - $\mathcal{W}aX$'s attribution, we model every transported instance pair (x, y) by the shift of its associated cluster, allowing us to formulate the problem of explanation as that of attributing $\sum_c \sum_{k \in c} \|\delta_c\|^2$. This quantity naturally decomposes into feature-wise relevances $R_i^c = \sum_{k \in c} (\delta_c)_i^2$ and instance-wise relevances $R_k^c = 1_{k \in c} \|\delta_c\|^2$. Results of this baseline attribution technique are shown in Fig. 3 (c).

Compared to U - $\mathcal{W}aX$, we observe that the clustering baseline produces maximal disentanglement in terms of *instances* (a consequence of the cluster-based formulation), but low feature-wise disentanglement, not clearly distinguishing between weight-related and size-related features.

Overall, this use case demonstrated the abilities of U - $\mathcal{W}aX$ to unravel a real-world shift of an aging process by only having access to distributions at two discrete times. Through its disentanglement capabilities U - $\mathcal{W}aX$ supplements $\mathcal{W}aX$ in producing more structured and insightful explanations of heterogeneous transport phenomena.

VII. USE CASE 2: INVESTIGATING DATASET DIFFERENCES

Selecting data sources is an essential aspect of learning an ML model. Thus, it is necessary to systematically evaluate in which way the various data sources differ (e.g. [53]) to detect, for example, whether one dataset under- or overrepresents specific subgroups. In this section, we show how U - $\mathcal{W}aX$ can be used to explore qualitatively the difference between two popular face datasets, namely ‘CelebA’ [54] and ‘Labeled Faces in the Wild’ (LFW) [55]. To focus on the semantically significant difference between the datasets, we apply rescaling to images so that the faces are centered and of the same size. We then randomly draw 10 000 examples from each dataset and feed them into a pretrained CLIP [56] model to generate latent features. Not only does the CLIP model produce a high-level abstract representation of images from which semantically interesting transport phenomena can be extracted, but the representation jointly expresses visual and textual features, enabling the characterization of the transport phenomena in terms of words. Our complete feature extraction pipeline involves center-cropping the LFW images to reduce background content (as CelebA images are already cropped to facial regions), applying the CLIP model’s prescribed preprocessing transforms, and normalizing each resulting embedding to unit norm.

We first apply our U - $\mathcal{W}aX$ method and search for a one-dimensional subspace that captures most variation in the

modeled transport to get an impression of the main transport trend. Specifically, we apply our method with parameters $C = 1$ and $r = 2$ in Eqs. (10) and (11), and set the subspace dimensionality to 1. The resulting subspace captures about 26% of the Wasserstein distance. Results of the analysis are shown in Fig. 4 (a), where we show the 16 coupled instances that maximally contribute to the Wasserstein distance as per Eq. (9b). From these instances, we see a transport trend where (young) females in CelebA get transported to (old) male faces in LFW, indicating that the two datasets distinctly represent the two subgroups. To get further insight into this transport trend, we leverage the joint representation space of CLIP and search for word vectors that maximally align with this subspace, specifically, with maximum cosine similarity. We search among the 20 000 most frequent Google terms⁴ (as also used by [57]). We observe that the most aligned words are on the one hand (female) celebrities, which is supported by multiple female names and words like ‘actresses’; on the other hand, politics-focused words, such as male politician names, ‘congressman’, and ‘grandfather’.

Aiming at obtaining finer and more structured insights into dataset differences, we apply the same method but choose $C = 100$ (with subspaces of one dimension) and $r = 3$ to extract a broader range of trends that are more specific to particular subsets of the data. These 100 subspaces capture 84% of the total contributions to the Wasserstein distance. Three of the learned subspaces are shown in Fig. 4 (b). Here, we show the coupled samples that most distinctly contribute to the Wasserstein distance through the particular subspace, specifically, having the maximum relevance ratio between the given subspace and the next most relevant subspace.

The first shown subspace, S_{59} , in Fig. 4 (b) appears to model a shift in wearing ‘eyewear’, which is characterized by the highest cosine similarities to related words and the visual characteristics of the strongest sample pairs (i.e. the lack of ‘glasses’ in the source set). This shift is relatively independent from the main female-to-male shift highlighted in (a), as the insertion of glasses does not come with substantial variation in the characteristics of the faces on which these glasses are inserted. Subspace S_{92} highlights another subtle difference between the CelebA and LFW datasets, where neutral faces, mostly of women, transport to similar-looking faces adorned with tennis-related items, such as rackets, balls, and outfits. The nature of this sub-shift is confirmed by words such as ‘tennis’, ‘wimbledon’, and ‘serena’ (a famous tennis player), exhibiting the highest cosine similarity to the subspace. As with the previous sub-shift, this sportswear sub-shift appears largely independent of the dominant shift, as coupled instances do not reveal additional differences. Looking now at the most strongly contributing examples in S_{96} , we see that LFW differentiates itself from CelebA by the presence of images containing more than one person. This observation is supported by the strong alignment of the subspace with corresponding text attributes like ‘couples’, indicating that the subspace aligns with the visual information provided by the highly relevant samples. If a classifier is trained on datasets with only a single visible face,

⁴<https://github.com/first20hours/google-10000-english>

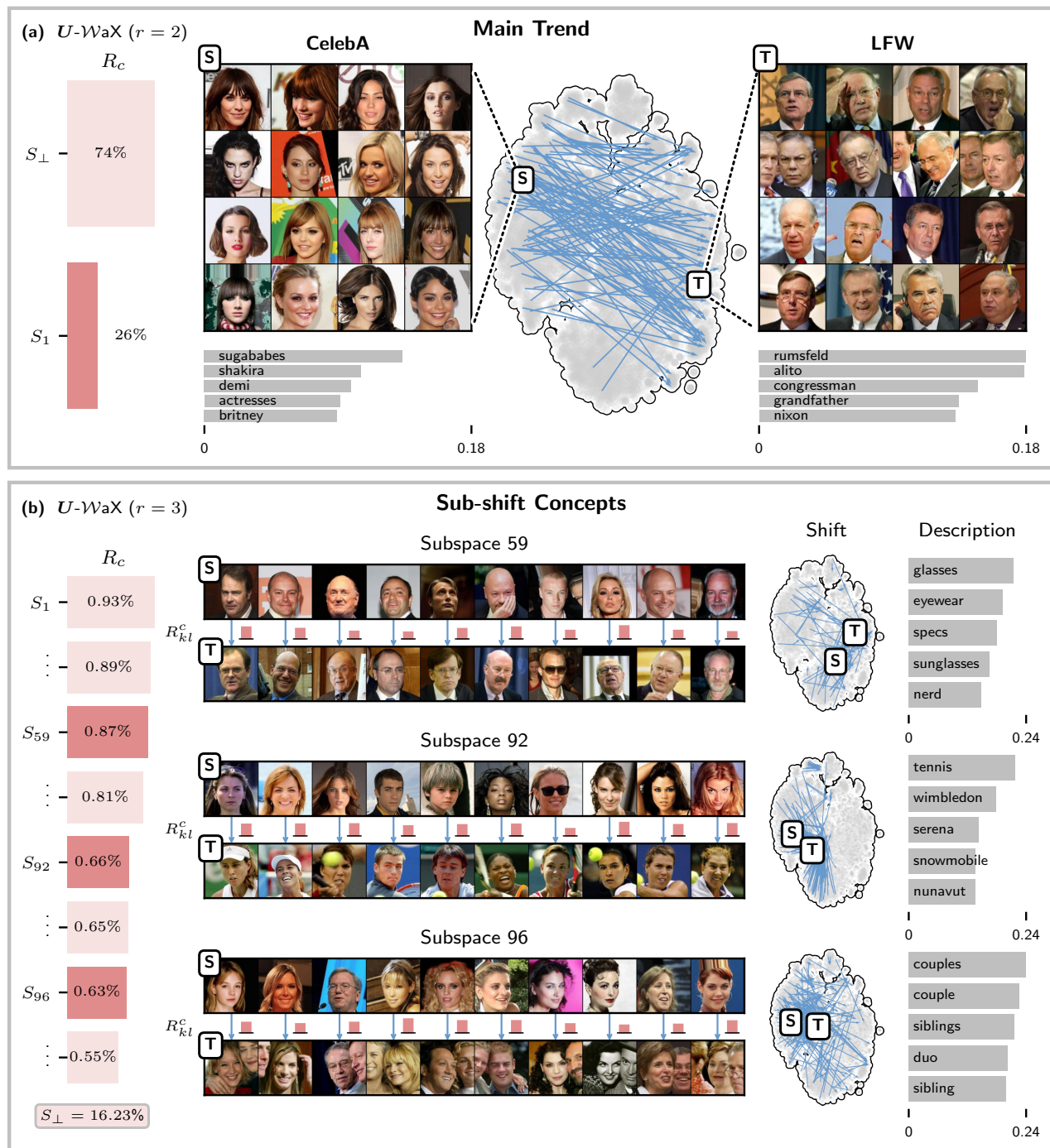


Fig. 4. Shift between the CelebA and LFW datasets as modeled by the Wasserstein distance ($p, q = 2$) and characterized by $U\text{-}W\alpha X$. We show $U\text{-}W\alpha X$ with $r = 2$ in (a) and with $r = 3$ in (b). While $r = 2$ provides a high-level/global view of the shift by modeling the main transport trend, $r = 3$ reveals diverse local sub-shifts. For ease of visualization, the subspace relevances R_c from Eq. (9a) are provided as an average over the intermediate range when labeled with vertical dots, and S_{\perp} indicates the unexplained residual relevance. The bars between the coupled samples indicate the sample relevance R_{kl}^c from Eq. (9b) within each subspace. For each subspace, we also show the t-SNE plots visualizing the localization and spread of the shifts, and the words with the highest absolute cosine similarity.

such samples can be ambiguous and cause wrong classifications upon deployment.

Overall, this use case has demonstrated how our method can help detect differences between datasets and present them interpretably to the user. We see such functionality as crucial

for dataset consolidation, a key step towards training better models and designing better evaluation benchmarks.

VIII. CONCLUSION

This work has addressed how to gain insight into real-world distribution shifts and transport phenomena. To this end, we

introduced WaX , a novel framework to explain Wasserstein distances—a popular tool for comparing distributions—by attributing them to distinct data components, such as individual features or instances. To the best of our knowledge, no other works have focused on attributing Wasserstein distances so far, and our work thereby fills a gap in the existing XAI literature. Our method is theoretically supported, computationally efficient, and shows broad applicability by flexibly adapting to various Wasserstein specifications and dataset types. We demonstrated our method’s high accuracy and utility through a comprehensive evaluation against a diverse set of baselines.

Our method is also designed to be interoperable with subspace analysis techniques, enabling the extension $U-WaX$, which disentangles Wasserstein models into multiple transport components. The usefulness of $U-WaX$ ’s disentangling capabilities was demonstrated in two realistic use cases: gaining insights into an abalone aging phenomenon, and uncovering subtle differences between two popular face datasets.

It is important to emphasize that our method does not directly describe the ground-truth transport phenomena but provides an interpretation of the Wasserstein distance used to model them. Consequently, any limitations of the Wasserstein model—such as its sensitivity to noise or its preference for least action—will be reflected in the resulting explanation. We therefore position our method as an interactive tool for practitioners: it can aid in validating a given transport model, choosing its hyperparameters, or developing more informed Wasserstein-based models. This, in turn, enables a more systematic and insightful analysis of the observed transport phenomena or dataset shift.

While we have focused in this work on classical optimal transport formulations, more advanced formulations that address their limitations (cf. [58]–[61]) should be explored in future work. This may include extending WaX to Gromov-Wasserstein distances [62] (and its extensions [63]), which allow transport across unregistered spaces, and that can also be expressed as a hierarchy of distances and norms. Furthermore, while our work has demonstrated the effectiveness of WaX at gaining insight into transport phenomena, achieving finer characterizations by adapting it to more advanced transport models, e.g. accounting for temporal dynamics and causality [64], appears to be another interesting future direction.

ACKNOWLEDGMENT

This work was in part supported by the Federal German Ministry for Education and Research (BMBF) under Grants BIFOLD24B, BIFOLD25B, 01IS18037A, 01IS18025A, and 01IS24087C.

REFERENCES

- [1] D. Klein, G. Palla, M. Lange, M. Klein, Z. Piran, M. Gander, L. Meng-Papaxanthos, M. Sterr, L. Saber, C. Jing, A. Bastidas-Ponce, P. Cota, M. Tarquis-Medina, S. Parikh, I. Gold, H. Lickert, M. Bakhti, M. Nitzan, M. Cuturi, and F. J. Theis, “Mapping cells through time and space with moscot,” *Nature*, vol. 638, no. 8052, pp. 1065–1075, Feb. 2025.
- [2] C. Villani, *Optimal Transport: Old and New*, ser. Grundlehren Der Mathematischen Wissenschaften. Springer Berlin Heidelberg, 2008.
- [3] G. Peyré and M. Cuturi, “Computational Optimal Transport,” Mar. 2020.

- [4] E. F. Montesuma, F. M. N. Mboula, and A. Souloumiac, “Recent advances in optimal transport for machine learning,” *IEEE Transactions on Pattern Analysis and Machine Intelligence*, vol. 47, no. 2, pp. 1161–1180, 2025.
- [5] M. Cuturi, “Sinkhorn Distances: Lightspeed Computation of Optimal Transport,” in *Advances in Neural Information Processing Systems*, vol. 26. Curran Associates, Inc., 2013, pp. 2292–2300.
- [6] S. Kulinski and D. I. Inouye, “Towards explaining distribution shifts,” in *ICML*, ser. Proceedings of Machine Learning Research, vol. 202. PMLR, 2023, pp. 17931–17952.
- [7] G. Montavon, W. Samek, and K.-R. Müller, “Methods for interpreting and understanding deep neural networks,” *Digital Signal Processing*, vol. 73, pp. 1–15, 2018.
- [8] D. Gunning and D. W. Aha, “DARPA’s explainable artificial intelligence (XAI) program,” *Ai Magazine*, vol. 40, no. 2, pp. 44–58, 2019.
- [9] W. Samek, G. Montavon, S. Lapuschkin, C. J. Anders, and K.-R. Müller, “Explaining Deep Neural Networks and Beyond: A Review of Methods and Applications,” *Proceedings of the IEEE*, vol. 109, no. 3, pp. 247–278, Mar. 2021.
- [10] A. Barredo Arrieta, N. Díaz-Rodríguez, J. Del Ser, A. Bennetot, S. Tabik, A. Barbado, S. García, S. Gil-Lopez, D. Molina, R. Benjamins, R. Chatila, and F. Herrera, “Explainable Artificial Intelligence (XAI): Concepts, taxonomies, opportunities and challenges toward responsible AI,” *Information Fusion*, vol. 58, pp. 82–115, Jun. 2020.
- [11] S. Lapuschkin, S. Wäldchen, A. Binder, G. Montavon, W. Samek, and K.-R. Müller, “Unmasking Clever Hans predictors and assessing what machines really learn,” *Nature Communications*, vol. 10, no. 1, p. 1096, Mar. 2019.
- [12] A. J. DeGrave, J. D. Janizek, and S.-I. Lee, “AI for radiographic COVID-19 detection selects shortcuts over signal,” *Nature Machine Intelligence*, vol. 3, no. 7, pp. 610–619, Jul. 2021.
- [13] J. Kauffmann, J. Dippel, L. Ruff, W. Samek, K.-R. Müller, and G. Montavon, “Explainable AI reveals Clever Hans effects in unsupervised learning models,” *Nature Machine Intelligence*, vol. 7, no. 3, pp. 412–422, Mar. 2025.
- [14] A. Binder, M. Bockmayr, M. Hägele, S. Wienert, D. Heim, K. Hellweg, M. Ishii, A. Stenzinger, A. Hocke, C. Denkert, K.-R. Müller, and F. Klauschen, “Morphological and molecular breast cancer profiling through explainable machine learning,” *Nature Machine Intelligence*, vol. 3, no. 4, pp. 355–366, 2021.
- [15] F. Klauschen, J. Dippel, P. Keyl, P. Jurmeister, M. Bockmayr, A. Mock, O. Buchstab, M. Alber, L. Ruff, G. Montavon, and K.-R. Müller, “Toward explainable artificial intelligence for precision pathology,” *Annual Review of Pathology: Mechanisms of Disease*, vol. 19, no. 1, pp. 541–570, 2024.
- [16] C. Zednik and H. Boelsen, “Scientific Exploration and Explainable Artificial Intelligence,” *Minds and Machines*, vol. 32, no. 1, pp. 219–239, Mar. 2022.
- [17] R. Roscher, B. Bohn, M. F. Duarte, and J. Garcke, “Explainable Machine Learning for Scientific Insights and Discoveries,” *IEEE Access*, vol. 8, pp. 42 200–42 216, 2020.
- [18] E. Štrumbelj and I. Kononenko, “Explaining prediction models and individual predictions with feature contributions,” *Knowledge and Information Systems*, vol. 41, no. 3, pp. 647–665, Dec. 2014.
- [19] S. M. Lundberg and S.-I. Lee, “A Unified Approach to Interpreting Model Predictions,” in *Advances in Neural Information Processing Systems*, vol. 30. Curran Associates, Inc., 2017.
- [20] S. Bach, A. Binder, G. Montavon, F. Klauschen, K.-R. Müller, and W. Samek, “On pixel-wise explanations for non-linear classifier decisions by layer-wise relevance propagation,” *PLOS ONE*, vol. 10, no. 7, pp. 1–46, Jul. 2015.
- [21] G. Montavon, A. Binder, S. Lapuschkin, W. Samek, and K.-R. Müller, “Layer-wise relevance propagation: An overview,” in *Explainable AI*, ser. Lecture Notes in Computer Science. Springer, 2019, vol. 11700, pp. 193–209.
- [22] B. Kim, M. Wattenberg, J. Gilmer, C. J. Cai, J. Wexler, F. B. Viégas, and R. Sayres, “Interpretability beyond feature attribution: Quantitative testing with concept activation vectors (TCAV),” in *ICML*, ser. Proceedings of Machine Learning Research, vol. 80. PMLR, 2018, pp. 2673–2682.
- [23] R. Achibat, M. Dreyer, I. Eisenbraun, S. Bosse, T. Wiegand, W. Samek, and S. Lapuschkin, “From attribution maps to human-understandable explanations through Concept Relevance Propagation,” *Nature Machine Intelligence*, vol. 5, no. 9, pp. 1006–1019, Sep. 2023.
- [24] P. Chormai, J. Herrmann, K.-R. Müller, and G. Montavon, “Disentangled explanations of neural network predictions by finding relevant subspaces,” *IEEE Transactions on Pattern Analysis and Machine Intelligence*, vol. 46, no. 11, pp. 7283–7299, 2024.
- [25] J. Quionero-Candela, M. Sugiyama, A. Schwaighofer, and N. D. Lawrence, *Dataset Shift in Machine Learning*. The MIT Press, 2009.

- [26] P. W. Koh, S. Sagawa, H. Marklund, S. M. Xie, M. Zhang, A. Balsubramani, W. Hu, M. Yasunaga, R. L. Phillips, I. Gao, T. Lee, E. David, I. Stavness, W. Guo, B. Earnshaw, I. S. Haque, S. M. Beery, J. Leskovec, A. Kundaje, E. Pierson, S. Levine, C. Finn, and P. Liang, “WILDS: A benchmark of in-the-wild distribution shifts,” in *ICML*, ser. Proceedings of Machine Learning Research, vol. 139. PMLR, 2021, pp. 5637–5664.
- [27] N. Courty, R. Flamary, D. Tuia, and A. Rakotomamonjy, “Optimal Transport for Domain Adaptation,” *IEEE Transactions on Pattern Analysis and Machine Intelligence*, vol. 39, no. 9, pp. 1853–1865, Sep. 2017.
- [28] K. Budhathoki, D. Janzing, P. Blöbaum, and H. Ng, “Why did the distribution change?” in *AISTATS*, ser. Proceedings of Machine Learning Research, vol. 130. PMLR, 2021, pp. 1666–1674.
- [29] N. Hulkund, N. Fusi, J. W. Vaughan, and D. Alvarez-Melis, “Interpretable Distribution Shift Detection using Optimal Transport,” Aug. 2022.
- [30] M. Sundararajan, A. Taly, and Q. Yan, “Axiomatic attribution for deep networks,” in *ICML*, ser. Proceedings of Machine Learning Research, vol. 70. PMLR, 2017, pp. 3319–3328.
- [31] C. Lin, M. Azabou, and E. L. Dyer, “Making transport more robust and interpretable by moving data through a small number of anchor points,” in *ICML*, ser. Proceedings of Machine Learning Research, vol. 139. PMLR, 2021, pp. 6631–6641.
- [32] M. Cuturi, M. Klein, and P. Abbelin, “Monge, bregman and occam: Interpretable optimal transport in high-dimensions with feature-sparse maps,” in *ICML*, ser. Proceedings of Machine Learning Research, vol. 202. PMLR, 2023, pp. 6671–6682.
- [33] H. Zhang, H. Singh, M. Ghassemi, and S. Joshi, “‘‘why did the model fail?’’: Attributing model performance changes to distribution shifts,” in *ICML*, ser. Proceedings of Machine Learning Research, vol. 202. PMLR, 2023, pp. 41 550–41 578.
- [34] T. Decker, A. Koehler, M. Lebacher, I. Thon, V. Tresp, and F. Buettner, “Explanatory model monitoring to understand the effects of feature shifts on performance,” in *KDD*. ACM, 2024, pp. 550–561.
- [35] J. Liu, T. Wang, P. Cui, and H. Namkoong, “On the Need for a Language Describing Distribution Shifts: Illustrations on Tabular Datasets,” in *Advances in Neural Information Processing Systems*, vol. 36. Curran Associates, Inc., Nov. 2023, pp. 51 371–51 408.
- [36] J. Gardner, Z. Popovic, and L. Schmidt, “Benchmarking distribution shift in tabular data with TableShift,” in *Advances in Neural Information Processing Systems*, vol. 36. Curran Associates, Inc., 2023, pp. 53 385–53 432.
- [37] G. Montavon, J. R. Kauffmann, W. Samek, and K.-R. Müller, “Explaining the predictions of unsupervised learning models,” in *xxAI@ICML*, ser. Lecture Notes in Computer Science. Springer, 2022, vol. 13200, pp. 117–138.
- [38] J. Kauffmann, M. Eiders, L. Ruff, G. Montavon, W. Samek, and K.-R. Müller, “From Clustering to Cluster Explanations via Neural Networks,” *IEEE Transactions on Neural Networks and Learning Systems*, vol. 35, no. 2, pp. 1926–1940, Feb. 2024.
- [39] L. You, L. Cao, and M. Nilsson, “DISCOUNT: Distributional Counterfactual Explanation With Optimal Transport,” Jan. 2024.
- [40] M. Serrurier, F. Mamalet, T. Fel, L. Béthune, and T. Boissin, “On the explainable properties of 1-Lipschitz Neural Networks: An Optimal Transport Perspective,” in *Advances in Neural Information Processing Systems*, vol. 36. Curran Associates, Inc., Nov. 2023, pp. 54 645–54 682.
- [41] D. Hill, J. Bone, A. Masoomi, M. Torop, and J. Dy, “Axiomatic explainer globalness via optimal transport,” in *AISTATS*, 2025.
- [42] R. R. Selvaraju, M. Cogswell, A. Das, R. Vedantam, D. Parikh, and D. Batra, “Grad-cam: Visual explanations from deep networks via gradient-based localization,” *Int. J. Comput. Vis.*, vol. 128, no. 2, pp. 336–359, 2020.
- [43] M. Ancona, E. Ceolini, C. Öztireli, and M. H. Gross, “Gradient-based attribution methods,” in *Explainable AI*, ser. Lecture Notes in Computer Science. Springer, 2019, vol. 11700, pp. 169–191.
- [44] A. Ali, T. Schnake, O. Eberle, G. Montavon, K.-R. Müller, and L. Wolf, “XAI for transformers: Better explanations through conservative propagation,” in *ICML*, ser. Proceedings of Machine Learning Research, vol. 162. PMLR, 2022, pp. 435–451.
- [45] S. Bluecher, J. Vielhaben, and N. Strodthoff, “Decoupling pixel flipping and occlusion strategy for consistent XAI benchmarks,” *Transactions on Machine Learning Research*, vol. 2024, 2024.
- [46] W. Samek, A. Binder, G. Montavon, S. Lapuschkin, and K.-R. Müller, “Evaluating the Visualization of What a Deep Neural Network Has Learned,” *IEEE Transactions on Neural Networks and Learning Systems*, vol. 28, no. 11, pp. 2660–2673, Nov. 2017.
- [47] A. Filiot, N. Dop, O. Tchita, A. Riou, R. Dubois, T. Peeters, D. Valter, M. Scalbert, C. Saillard, G. Robin, and A. Olivier, “Distilling foundation models for robust and efficient models in digital pathology,” 2025.
- [48] O. Ciga, T. Xu, and A. L. Martel, “Self supervised contrastive learning for digital histopathology,” *Machine Learning with Applications*, vol. 7, p. 100198, Mar. 2022.
- [49] A. Filiot, R. Ghermi, A. Olivier, P. Jacob, L. Fidon, A. Camara, A. M. Kain, C. Saillard, and J.-B. Schiratti, “Scaling Self-Supervised Learning for Histopathology with Masked Image Modeling,” p. 2023.07.21.23292757, Dec. 2024.
- [50] R. J. Chen, T. Ding, M. Y. Lu, D. F. K. Williamson, G. Jaume, A. H. Song, B. Chen, A. Zhang, D. Shao, M. Shaban, M. Williams, L. Oldenburg, L. L. Weishaupt, J. J. Wang, A. Vaidya, L. P. Le, G. Gerber, S. Sahai, W. Williams, and F. Mahmood, “Towards a general-purpose foundation model for computational pathology,” *Nature Medicine*, vol. 30, no. 3, pp. 850–862, Mar. 2024.
- [51] S. Haufe, F. Meinecke, K. Görgen, S. Dähne, J.-D. Haynes, B. Blankertz, and F. Bießmann, “On the interpretation of weight vectors of linear models in multivariate neuroimaging,” *NeuroImage*, vol. 87, pp. 96–110, 2014.
- [52] W. Nash, T. Sellers, S. Talbot, A. Cawthorn, and W. Ford, “Abalone,” <https://doi.org/10.24432/C55C7W>, Nov. 1995.
- [53] D. Alvarez-Melis and N. Fusi, “Geometric dataset distances via optimal transport,” in *Advances in Neural Information Processing Systems*, vol. 33. Curran Associates, Inc., 2020, pp. 21 428–21 439.
- [54] Z. Liu, P. Luo, X. Wang, and X. Tang, “Deep learning face attributes in the wild,” in *ICCV*. IEEE Computer Society, 2015, pp. 3730–3738.
- [55] G. B. Huang, M. Ramesh, T. Berg, and E. Learned-Miller, “Labeled faces in the wild: A database for studying face recognition in unconstrained environments,” University of Massachusetts, Amherst, Tech. Rep. 07-49, Oct. 2007.
- [56] A. Radford, J. W. Kim, C. Hallacy, A. Ramesh, G. Goh, S. Agarwal, G. Sastry, A. Askell, P. Mishkin, J. Clark, G. Krueger, and I. Sutskever, “Learning transferable visual models from natural language supervision,” in *ICML*, ser. Proceedings of Machine Learning Research, vol. 139. PMLR, 2021, pp. 8748–8763.
- [57] T. P. Oikarinen and T. Weng, “Clip-dissect: Automatic description of neuron representations in deep vision networks,” in *ICLR*. OpenReview.net, 2023.
- [58] D. Alvarez-Melis, T. S. Jaakkola, and S. Jegelka, “Structured optimal transport,” in *AISTATS*, ser. Proceedings of Machine Learning Research, vol. 84. PMLR, 2018, pp. 1771–1780.
- [59] L. Chizat, G. Peyré, B. Schmitzer, and F.-X. Vialard, “Scaling algorithms for unbalanced optimal transport problems,” *Math. Comput.*, vol. 87, no. 314, pp. 2563–2609, 2018.
- [60] L. Chapel, M. Z. Alaya, and G. Gasso, “Partial Optimal Transport with applications on Positive-Unlabeled Learning,” in *Advances in Neural Information Processing Systems*, vol. 33. Curran Associates, Inc., 2020, pp. 2903–2913.
- [61] D. Mukherjee, A. Guha, J. M. Solomon, Y. Sun, and M. Yurochkin, “Outlier-robust optimal transport,” in *ICML*, ser. Proceedings of Machine Learning Research, vol. 139. PMLR, 2021, pp. 7850–7860.
- [62] F. Mémoli, “Gromov-Wasserstein Distances and the Metric Approach to Object Matching,” *Foundations of Computational Mathematics*, vol. 11, no. 4, pp. 417–487, Aug. 2011.
- [63] V. Titouan, I. Redko, R. Flamary, and N. Courty, “CO-optimal transport,” in *Advances in Neural Information Processing Systems*, H. Larochelle, M. Ranzato, R. Hadsell, M. Balcan, and H. Lin, Eds., vol. 33. Curran Associates, Inc., 2020, pp. 17 559–17 570.
- [64] D. Bartl, M. Beiglböck, and G. Pammer, “The Wasserstein space of stochastic processes,” *Journal of the European Mathematical Society*, Dec. 2024.

Wasserstein Distances Made Explainable: Insights into Dataset Shifts and Transport Phenomena

(SUPPLEMENTARY NOTES)

Philip Naumann Jacob Kauffmann Grégoire Montavon

This document contains supplementary notes that provide more details on the content of the main text “Wasserstein Distances Made Explainable: Insights into Dataset Shifts and Transport Phenomena”. We provide additional proofs, derivations, figures, and experimental details to support the main text’s conceptual, technical, and experimental parts.

Supplementary Note A: Sensitivity of Explanations to the Wasserstein Model

In this note, we provide qualitative results showing how $\mathcal{W}aX$ ’s attribution exhibits better sensitivity to the specification of the Wasserstein model than the actual transport map. Two examples are shown in Fig. 1. In the first example, we consider a transport phenomenon of an incompressible fluid moving from left to right and passing through a bottleneck. While different specifications of the Wasserstein distance lead to roughly the same transport solution, the key contributors to the Wasserstein distance change drastically, with the bottleneck playing an increasingly important role with large values of p . This increasingly important role is faithfully reflected in explanations produced by $\mathcal{W}aX$, whereas the data, its coupling, and derived explanations are largely insensitive. In the second example, building on a real dataset and attributing this time on input features, similar high sensitivity of our $\mathcal{W}aX$ method compared to the coupling distribution is highlighted, with the most relevant features changing significantly whether we consider \mathcal{W}_1 or \mathcal{W}_4 .

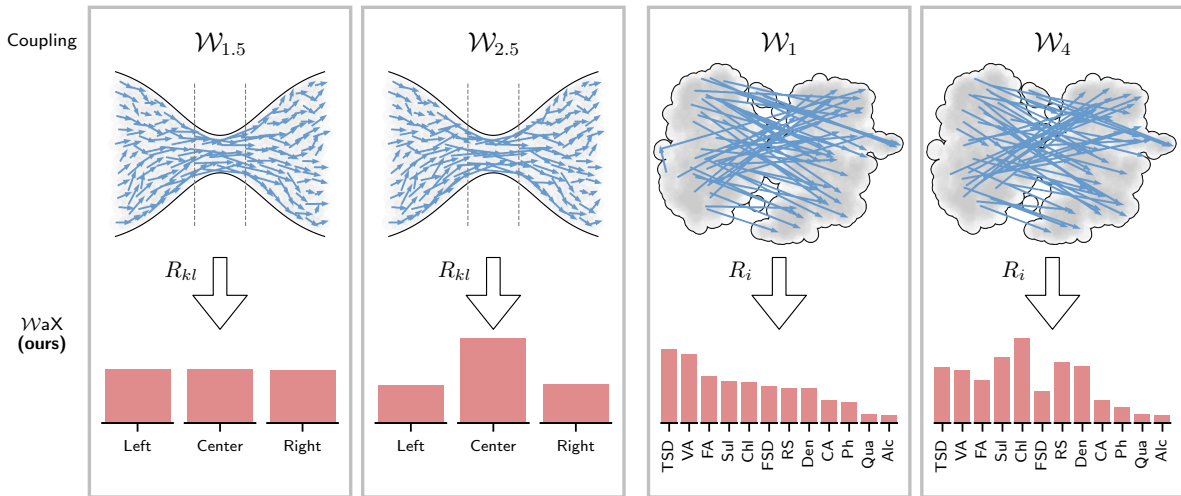


Figure 1: On the left, rightward shift of an incompressible fluid through a bottleneck by identifying the contributions of points (cf. Eq. (3a) from the main text) before, in, and after a bottleneck to the Wasserstein distance. On the right, $\mathcal{W}aX$ identifies features that contribute to the shift between red and white wine in terms of input features (cf. Eq. (3b) from the main text). The arrows visualizing the coupling distribution are clustered (cf. [1]) for ease of visualization.

Supplementary Note B: Proofs of Propositions 1 and 2

In this note, we provide the mathematical derivations supporting Propositions 1 and 2 from the main text. Specifically, we show how the relevance scores R_{kl} and R_i align with gradient-based computations under the choice of hyperparameters $\alpha = p$ and $\beta = q$, respectively.

Proposition 1. *When choosing $\alpha = p$, the relevance scores R_{kl} of pairs of points can be expressed as the gradient computation $R_{kl} = (\partial\mathcal{W}_p/\partial z_{kl}) \cdot z_{kl}$, where we treat γ^* as a constant.*

Proof.

$$\begin{aligned} \frac{\partial\mathcal{W}_p}{\partial z_{kl}} \cdot z_{kl} &= \left(\frac{\partial}{\partial z_{kl}} \left(\sum_{ij} \gamma_{ij}^* \cdot z_{ij}^p \right)^{1/p} \right) \cdot z_{kl} \\ &= \left(\left(\sum_{ij} \gamma_{ij}^* \cdot z_{ij}^p \right)^{1/p-1} \cdot \gamma_{kl}^* \cdot z_{kl}^{p-1} \right) \cdot z_{kl} \\ &= \frac{\gamma_{kl}^* \cdot z_{kl}^p}{\sum_{kl} \gamma_{kl}^* \cdot z_{kl}^p} \mathcal{W}_p \\ &= R_{kl} \end{aligned}$$

□

Proposition 2. *When choosing $\alpha = p$ and $\beta = q$, the relevance scores R_i of the input features can be expressed as the gradient computation $R_i = (\partial\mathcal{W}_p/\partial x_{:,i})^\top x_{:,i} + (\partial\mathcal{W}_p/\partial y_{:,i})^\top y_{:,i}$, where γ^* is again treated as constant.*

Proof. First, note that for any pair (x, y) and $0 < q < \infty$ we can expand as follows:

$$\begin{aligned} \frac{\partial\|x-y\|_q}{\partial x_i} \cdot x_i + \frac{\partial\|x-y\|_q}{\partial y_i} \cdot y_i &= \left(\sum_i |x_i - y_i|^q \right)^{\frac{1}{q}-1} \cdot |x_i - y_i|^{q-1} \cdot (x_i \cdot \text{sgn}(x_i - y_i) + y_i \cdot \text{sgn}(y_i - x_i)) \\ &= \frac{|x_i - y_i|^q}{\sum_i |x_i - y_i|^q} \cdot \|x - y\|_q \end{aligned}$$

where sgn is the sign function. Next, we apply the chain rule and use Proposition 1 from the main text as an intermediate step:

$$\begin{aligned} \frac{\partial\mathcal{W}_p}{\partial x_{:,i}}^\top x_{:,i} + \frac{\partial\mathcal{W}_p}{\partial y_{:,i}}^\top y_{:,i} &= \sum_{kl} \frac{\partial\mathcal{W}_p}{\partial z_{kl}} \cdot \left(\frac{\partial z_{kl}}{\partial x_{k,i}} x_{k,i} + \frac{\partial z_{kl}}{\partial y_{l,i}} y_{l,i} \right) \\ &= \sum_{kl} \frac{R_{kl}}{z_{kl}} \cdot \left(\frac{|x_{k,i} - y_{l,i}|^q}{\sum_i |x_{k,i} - y_{l,i}|^q} \cdot z_{kl} \right) \\ &= \sum_{kl} \frac{|x_{k,i} - y_{l,i}|^q}{\sum_i |x_{k,i} - y_{l,i}|^q} \cdot R_{kl} \\ &= R_i \end{aligned}$$

□

Supplementary Note C: Choosing WaX Hyperparameters

This note empirically supports the choice of our proposed WaX α, β -hyperparameter heuristic as proposed in Section III from the main text:

$$\begin{aligned} \alpha &= p \\ \beta &= \min(p + 2, q) \end{aligned}$$

assuming $p \ll \infty$. We use the ‘Mice’ dataset [2] due to its high dimensionality. We iterate over different model parameters p and q , and explanation parameters α and β to study how they influence the SRG metric (Eq. (5) from the main text). We see in Fig. 2 that our heuristic for choosing α and β (blue marker) is always within or close to the optimal parameter area in terms of SRG score (yellow), as visualized by the contour lines.

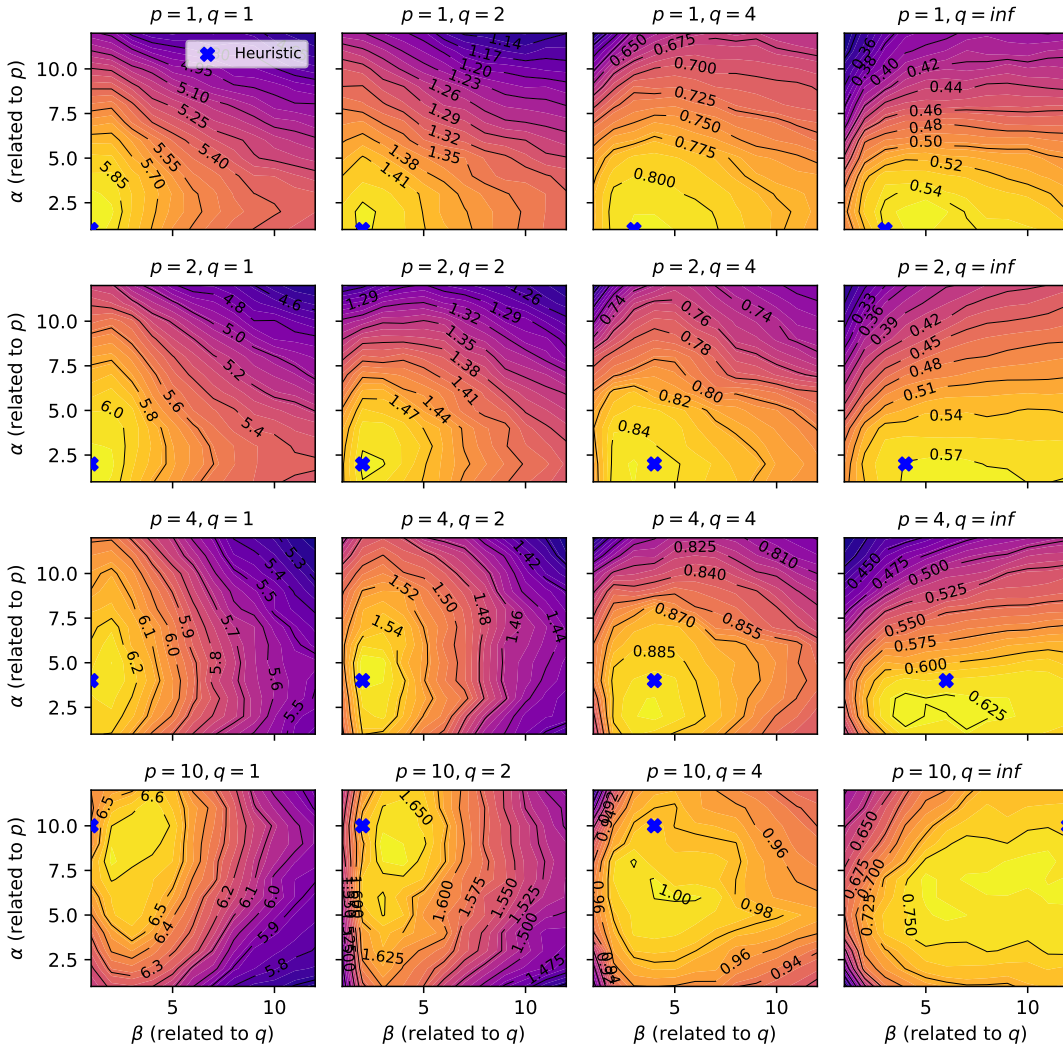


Figure 2: Effect of WaX hyperparameters (α and β) on the SRG performance metric (Eq. (5) from the main text) for various specifications of the Wasserstein distance (parameters p and q) and applied to the ‘Mice’ dataset. The highest SRG values are shown in yellow. Each plot shows our heuristic for choosing the hyperparameters α and β as an annotated blue marker.

Supplementary Note D: Datasets Used and Preprocessing

All tabular datasets used in Tables I and III and Section VI from the main text are taken from the “UCI machine learning repository” [3].

In *Section IV-A* from the main text, the tabular datasets were preprocessed by retaining only real-valued features, removing features and instances with a high proportion of missing values, eliminating duplicate instances, removing strong outliers where any feature value deviates more than three standard deviations from its mean, standardizing features to zero mean and unit variance, and imputing remaining missing values using nearest-neighbor imputation. In the case of the ‘Crime’ dataset [4], we only use the features considered in [13] as the starting point (hence the much lower number in Table I from the main text in comparison to the original dataset in Table 1).

In *Section IV-B* from the main text, the time series datasets are similarly preprocessed as in Section IV-A from the main text. We remove features with too many missing values and samples with any missing values, removing strong outliers where any feature value deviates more than three standard deviations from its mean, and standardizing to zero mean and unit variance. When a sample

Section	Dataset	N	d	Missing Values	Ref.
IV-A	Crime	1994	127	✓	[4]
	Mice	1080	80	✓	[2]
	Musks1	476	168	-	[5]
	Robot	463	90	-	[6]
	Wine	4898	12	-	[7]
	Wisconsin	569	30	-	[8]
IV-B	Air Quality	9358	15	✓	[9]
	Electricity	2 075 259	9	✓	[10]
	Appliances	19 735	28	-	[11]
VI	Abalone	4177	8	-	[12]

Table 1: Tabular datasets used in the main text. The number of samples N and dimensions d refer to the *original* datasets. The values after preprocessing (e.g. removing categorical features, missing values, outliers, etc.) used in the experiments can be found in the main text tables.

is eliminated in this process, we also delete its corresponding coupled match to ensure that we always have ground-truth couplings.

In *Section VI* from the main text, we remove the categorical ‘sex’ feature from the Abalone dataset. Then, we standardize the remaining features to zero mean and unit variance. Finally, we remove strong outliers, i.e. those where any feature value deviates more than three standard deviations from its mean, to prevent them from spuriously influencing the subsequent analysis.

Supplementary Note E: Experimental Details for Section IV-B

The evaluation is performed over three different time series datasets (see Table 1 in Supplementary Note D), with temporal shifts Δt ranging from 1 to 6, and results are averaged over all source times $t \in \{0, \dots, 23\}$. Our WaX method is applied with two Wasserstein distance models, the classical one (with coupling γ^*) and a maximally regularized [14] one (with coupling $\gamma_{\text{reg}}^* = \text{cst.}$).

We create subset splits $\tilde{\mathcal{D}}_{\mathcal{S}} = \{(x_{t+kT})\}_{k \in \mathcal{K}_1}$ and $\tilde{\mathcal{D}}_{\mathcal{T}} = \{(x_{t+\Delta t+kT})\}_{k \in \mathcal{K}_2}$ to avoid exposing the ground truth coupling. These are subsets of the original data $\mathcal{D}_{\mathcal{S}}$ and $\mathcal{D}_{\mathcal{T}}$, respectively, with \mathcal{K}_1 and \mathcal{K}_2 being disjoint, thus defining a random partition of \mathbb{Z} . This setup simulates a scenario where WaX has access to the data distributions but not the exact same instances evolving from source to target. In our evaluation benchmark, we only use time delays less than or equal to six hours to guarantee reasonable mutual information between source and target. We only retain cases where at least 50 source and target instances are available for characterizing the transport.

For the experiments on the PLISM dataset [15], we also partition the data into random, non-overlapping subsets for the evaluated methods.

Supplementary Note F: Attributing KL Divergence

In this note, we provide the mathematical details for attributing the Kullback-Leibler (KL) divergence, as discussed in Section IV-B from the main text.

We first consider the case where the source and target distributions are isotropic Gaussian (or modeled as such), specifically:

$$\begin{aligned}\mu(x) &= \mathcal{N}(m, \sigma^2 I) \\ \nu(x) &= \mathcal{N}(-m, \sigma^2 I)\end{aligned}$$

We get the following expression for the KL divergence:

$$\begin{aligned}
D_{\text{KL}}(\mu \parallel \nu) &= \mathbb{E}_{\mu} \left[\log \frac{\mu(x)}{\nu(x)} \right] \\
&= \mathbb{E}_{\mu} \left[-\frac{1}{2\sigma^2} \|x - m\|^2 + \frac{1}{2\sigma^2} \|x + m\|^2 \right] \\
&= \mathbb{E}_{\mu} \left[2 \frac{x^{\top} m}{\sigma^2} \right] \\
&= \frac{2\|m\|^2}{\sigma^2}
\end{aligned}$$

Likewise, we get

$$\begin{aligned}
D_{\text{KL}}(\nu \parallel \mu) &= \mathbb{E}_{\nu} \left[\log \frac{\nu(x)}{\mu(x)} \right] \\
&= \frac{2\|m\|^2}{\sigma^2}
\end{aligned}$$

The symmetrized KL divergence can be attributed to the input features as:

$$\mathcal{E}\{D_{\text{KL}}(\mu \parallel \nu) + D_{\text{KL}}(\nu \parallel \mu)\}_i = 4 \frac{m_i^2}{\sigma^2}$$

In other words, attribution is proportional to the square difference between the source and target means along each dimension and is also equivalent to attribution of a mean shift.

When classifying the data using a logistic classifier (including nonlinear versions of it), and assuming that source and target distributions are given the same weight during training, the output of the classifier $f(x)$ is interpretable as the log-density ratio $\log[\mu(x)/\nu(x)]$. This gives:

$$\begin{aligned}
D_{\text{KL}}(\mu \parallel \nu) &= \mathbb{E}_{\mu} \left[\log \frac{\mu(x)}{\nu(x)} \right] \\
&= \mathbb{E}_{\mu}[f(x)]
\end{aligned}$$

and similarly

$$\begin{aligned}
D_{\text{KL}}(\nu \parallel \mu) &= \mathbb{E}_{\nu} \left[\log \frac{\nu(x)}{\mu(x)} \right] \\
&= \mathbb{E}_{\nu}[-f(x)]
\end{aligned}$$

where f is a model (e.g. a logistic classifier or a neural network). Attribution of the symmetrized KL-divergence thus proceeds as:

$$\mathcal{E}\{D_{\text{KL}}(\mu \parallel \nu) + D_{\text{KL}}(\nu \parallel \mu)\}_i = \mathbb{E}_{\mu}[\mathcal{E}\{f(x)\}_i] + \mathbb{E}_{\nu}[\mathcal{E}\{-f(x)\}_i]$$

The attribution of the classifier logit $f(x)$ can be carried out using existing attribution techniques such as LRP (cf. [16, 17]). When f is a linear classifier, i.e. $f(x) = w^{\top}x + b$, GI becomes a mean shift weighted by w : $R_i = \mathbb{E}_{\mu}[w_i x_i] + \mathbb{E}_{\nu}[-w_i x_i] = w_i(\mathbb{E}_{\mu}[x_i] - \mathbb{E}_{\nu}[x_i]) = w_i(\bar{x}_i - \bar{y}_i)$, where \bar{x} and \bar{y} are source and target mean. Another attribution scheme uses the sensitivity of the function, i.e. $R_i = \left| \frac{\partial f}{\partial x_i} \right|^p = |w_i|^p$ with $p \geq 1$.

Supplementary Note G: Closed Form Solution for U -WaX

This note provides a closed-form solution for U -WaX in the special case of $r = 2$ and $C = 1$. For this special case, the orthogonal matrix used for modeling subspaces in Section V from the main text reduces to a two-block matrix

$$\mathbf{U} = (\mathbf{U} \mid \mathbf{U}_{\perp}) \tag{1}$$

where U is the subspace we would like to optimize and U_{\perp} is the orthogonal complement. The U -WaX objective similarly reduces to a measure of the spread of shifts expressed in the given subspace:

$$Q = \left(\sum_{kl} \gamma_{kl}^* \cdot z_{kl}^2 \right)^{1/2} \quad (2)$$

$$\text{where } z_{kl} = \|U^{\top}(x_k - y_l)\|_2 \quad (3)$$

It can then be shown that the optimization problem can be carried out in closed form:

$$\begin{aligned} \operatorname{argmax}_U \{Q\} &= \operatorname{argmax}_U \{Q^2\} \\ &= \operatorname{argmax}_U \left\{ \sum_{kl} \gamma_{kl}^* \cdot \|U^{\top}(x_k - y_l)\|_2^2 \right\} \\ &= \operatorname{argmax}_U \{ \operatorname{Tr}(U^{\top} S U) \} \end{aligned}$$

subject to $U^{\top}U = I$, and where $S = \sum_{kl} \gamma_{kl}^* (x_k - y_l)(x_k - y_l)^{\top}$. This is a canonical form similar to that of PCA, where the subspace U spans the leading eigenvectors of the matrix S .

Interestingly, PCA can be seen as a special case of the problem above where the target instances are set to the mean source instances (i.e. $y_l = \bar{x}$). This special case can be interpreted as the subspace that maximally expresses the transport of source data points to their means or vice versa.

References

- [1] S. Kulinski and D. I. Inouye. Towards explaining distribution shifts. In *ICML*, volume 202 of *Proceedings of Machine Learning Research*, pages 17931–17952. PMLR, 2023.
- [2] C. Higuera, K. J. Gardiner, and K. J. Cios. Mice protein expression. <https://doi.org/10.24432/C50S3Z>, August 2015.
- [3] M. Kelly, R. Longjohn, and K. Nottingham. The UCI machine learning repository. <https://archive.ics.uci.edu>, 2023.
- [4] M. Redmond. Communities and crime. <https://doi.org/10.24432/C53W3X>, July 2009.
- [5] D. Chapman and A. N. Jain. Musk (version 1). <https://doi.org/10.24432/C5ZK5B>, September 1994.
- [6] L. S. Lopes and L. M. Camarinha-Matos. Robot execution failures. <https://doi.org/10.24432/C5M89N>, April 1999.
- [7] P. Cortez, A. Cerdeira, F. Almeida, T. Matos, and J. Reis. Wine quality. <https://doi.org/10.24432/C56S3T>, October 2009.
- [8] W. H. Wolberg, O. L. Mangasarian, and W. N. Street. Breast cancer wisconsin (diagnostic). <https://doi.org/10.24432/C5DW2B>, October 1995.
- [9] S. D. Vito. Air quality. <https://doi.org/10.24432/C59K5F>, March 2016.
- [10] G. Hébrail and A. Berard. Individual household electric power consumption. <https://doi.org/10.24432/C58K54>, August 2012.
- [11] L. Candanedo. Appliances energy prediction. <https://doi.org/10.24432/C5VC8G>, February 2017.
- [12] W. Nash, T. Sellers, S. Talbot, A. Cawthorn, and W. Ford. Abalone. <https://doi.org/10.24432/C55C7W>, November 1995.

- [13] J. Gardner, Z. Popovic, and L. Schmidt. Benchmarking distribution shift in tabular data with TableShift. In *Advances in Neural Information Processing Systems*, volume 36, pages 53385–53432. Curran Associates, Inc., 2023.
- [14] M. Cuturi. Sinkhorn Distances: Lightspeed Computation of Optimal Transport. In *Advances in Neural Information Processing Systems*, volume 26, pages 2292–2300. Curran Associates, Inc., 2013.
- [15] A. Filiot, N. Dop, O. Tchita, A. Riou, R. Dubois, T. Peeters, D. Valter, M. Scalbert, C. Saillard, G. Robin, and A. Olivier. Distilling foundation models for robust and efficient models in digital pathology, 2025.
- [16] S. Bach, A. Binder, G. Montavon, F. Klauschen, K.-R. Müller, and W. Samek. On pixel-wise explanations for non-linear classifier decisions by layer-wise relevance propagation. *PLOS ONE*, 10(7):1–46, July 2015.
- [17] G. Montavon, A. Binder, S. Lapuschkin, W. Samek, and K.-R. Müller. Layer-wise relevance propagation: An overview. In *Explainable AI*, volume 11700 of *Lecture Notes in Computer Science*, pages 193–209. Springer, 2019.